Study of the inter-strip gap effects on the response of Double Sided Silicon Strip Detectors using proton micro-beams

Published version:

DOI:10.1016/j.nima.2014.08.009

(Article begins on next page)

Study of the inter-strip gap effects on the response of Double Sided Silicon Strip Detectors using proton micro-beams

Nuclear Instruments and Methods in Physics Research A 767 (2014) 99–111

L. Grassi, J. Forneris, D. Torresi, L. Acosta, A. Di Pietro, P. Figuera, M. Fisichella, V. Grilj, M. Jakšić, M. Lattuada, T. Mijatović, M. Milin, L. Prepolec, N. Skukan, N. Soić, V. Tokić, M. Uroić

Study of the inter-strip gap effects on the response of Double Sided Silicon Strip Detectors using proton micro-beams

L. Grassi[a,*], J. Forneris[b], D. Torresi[c], L. Acosta[c,d], A. Di Pietro[c], P. Figuera[c], M. Fisichella[c], V. Grilj[a], M. Jakšić[a], M. Lattuada[c,e], T. Mijatović[a], M. Milin[f], L. Prepolec[a], N. Skukan[a], N. Soić[a], V. Tokić[a], M. Uroić[a]

[a] *Ruđer Bošković Institute, Zagreb, Croatia*
[b] *Physics Department, NIS Centre and CNISM, University of Torino; INFN sez. Torino, Torino, Italy*
[c] *INFN, Laboratori Nazionali del Sud, Catania, Italy*
[d] *Departamento de Física Aplicada. Universidad de Huelva, Huelva, Spain*
[e] *Dipartimento di Fisica e Astronomia, Università di Catania, Catania, Italy*
[f] *Department of Physics, Faculty of Science, University of Zagreb, Zagreb, Croatia*

Abstract

Double Sided Silicon Strip Detectors (DSSSDs) are segmented silicon detectors widely used for the detection of charged particles. When a charged particle hits the gap between two adjacent strips, a signal, different from the full energy one, can be generated, resulting in an incorrect energy information. With the purpose of studying inter-strip effects on the detector response, an experiment was performed using a proton micro-beam. The response of two DSSSDs, 75 and 998 μm thick, was measured as a function of the proton impact position, beam energy and bias voltage using a low intensity proton micro-beam, of about few hundred particles per second (pps). Results show that the effective width of the inter-strip region,which in turn is related to the efficiency for full energy detection, varies with both detected energy and bias voltage. The experimental results are interpreted within a simplified model.

Keywords: Strip detector, DSSSD, inter-strip gap, proton micro-beam

*Corresponding author
Email address: laura.grassi@irb.hr (L. Grassi)

1. Introduction

Segmented silicon detectors have been introduced for charged particle detection more than 25 years ago and they have gained a central role in high-energy physics. Nowadays they are in standard use also in low energy nuclear physics experiments, both for structure and dynamics studies, when reaction products have to be detected with good energy and angular resolution in a large solid angle.

The segmented geometry allows accurate measurement of the emission direction, crucial information in experiments aiming to study angular distributions of various processes (e.g. [1–4]), or for the coincident detection of two or more charged reaction products, with the goal to fully characterize the final state of the interaction process (e.g. [5]). Such detectors are also commonly used in unbound state spectroscopy studies using the inverse kinematics thick target scattering method e.g. [6, 7]. They are particularly suitable for experiments with low intensity radioactive ion beams and for measurements of very low cross-section processes with stable beams.

A DSSSD is a silicon detector with both electrodes (front and back side) segmented into strips. If N_f and N_b are the number of strips on the front (junction) and back (ohmic) side respectively, such detector provides information on $N_f \times N_b$ pixels (overlap regions between front and back strips) by using just $N_f + N_b$ electronics channels. Therefore, both sides have several strip-to-strip separation regions, called "inter-strip gaps" in the following. The DSSSD response to a charged particle provides information on its 2-dimensional position of incidence and on the deposited energy. When electron-hole (e-h) pairs created by the ion within the volume of the detector move along the electric-field lines, they induce currents on the electrodes. For particles hitting the central region of the pixel, a signal carrying information on the correct deposited energy in the detector originates only from those two strips that define the considered pixel. On the other hand, it has been observed that ions entering the detector through an inter-strip gap lead to phenomena such as charge-sharing and inverted polarity signals [8–15].

Previous studies of the inter-strip effects on the response of segmented Si detectors were performed by using α-particles of low energies [14, 15], 3 MeV protons [15], 59.5 keV γ-rays from an ^{241}Am source [12], laser beams [8, 13] and, more recently, beams of ^{7}Li and ^{16}O ions of energies between 6 and 50 MeV [11]. The study [11], using ^{7}Li and ^{16}O ion beams, focused on the DSSSD efficiency for full energy detection, defined as the ratio between the number of events measured with the correct full energy and the total number of detected events. It was shown that this efficiency depends on the energy of the detected ion and on the applied bias voltage. In addition, it was found that the measured efficiency is lower than the value extracted by simply considering the geometrical width of the inter-strip gap. This means that the width of the inter-strip region, where the energy of the impinging ions is not correctly measured, is different than the geometrical inter-strip width given in the detector specifications.

In principle, the knowledge on the inter-strip width makes possible an *a priori* calculation of the DSSSD efficiency for full energy detection of various ions for a range of energies, a crucial information for those experiments where absolute cross section measurements are performed. This finding therefore motivated the present study, aiming to perform systematic measurements of the effective width of the inter-strip gap and to improve the understanding of the physical effects occurring there, leading to reduced amplitude signals and corresponding efficiency variations.

In this paper, we report results of an experiment performed at the Ruđer Bošković Institute (RBI), in which two DSSSDs with different thickness (75 and 998 μm) were characterized by the Ion Beam Induced Charge (IBIC) technique, i.e. by scanning different inter-strip regions with a proton micro-beam and recording the energy pulses along with the spatial coordinates of the impinging proton on the detector surface. Proton beam energies of 800, 1700, 3000 and 6000 keV were selected for probing inter-strip effects at different penetration depths (see table 1). Beam currents of the order of few hundred particles per second (pps) have been used in the measurements.

Table 1: Proton beam energies used in measurements with the two DSSSDs and their corresponding range in silicon.

Proton energy(keV)	Proton range in silicon (μm)	DSSSD irradiated (μm)
800	10	75
1700	35	75 & 998
3000	90	75 (punch through)
6000	295	998

The paper is organized as follows. Section 2 describes the experimental set-up and methodology. In Section 3, the experimental results are presented separately for each detector. The theoretical model and interpretation of the results is presented in Section 4. Finally, Section 5 summarizes the obtained results.

2. Experimental methodology

2.1. Micro-beam setup

In the last decade, upgrades of the RBI micro-probe facility resulted in the improvement of its focusing system, construction of a versatile spherical scattering chamber, good selection of detectors for different characterization techniques and development of a digital data acquisition system. Since ion beams from either 1 MV or 6 MV tandem accelerators can be injected into the micro-probe beam line, a wide selection of ions can be used for the application of the Ion Beam Induced Charge technique. In the case of the 6 MV Tandem Van de Graaff accelerator used in this work, two negative ion sources, namely

Alphatross (used for production of hydrogen and helium ions) and sputtering (used for a wide range of elements such as hydrogen, lithium, carbon, oxygen, silicon, chlorine and others) are available. Ion beam transport and accelerator operation is computer controlled by a custom software based on the Test Point package [16–18].

In the present experiment, the ion beam focusing was performed with an Oxford triplet configuration, which is suitable for light ions with $E \cdot m/C^2$ of up to 8 MeV A/C^2 where A is the mass number and C the charge of the accelerated ion. Higher rigidity ions can also be focused, however this is done with a quintuplet configuration or a longer working distance (260 mm) doublet.

Application of the IBIC technique for detector testing implies the use of very low micro-beam intensities of few hundreds of pps. This is achieved by significant reduction of both the object and collimator apertures. Owing to the corresponding reduction of beam divergence, the influence of the ion optical system aberrations was also minimized and a typical micro-beam spatial resolution of less than 1 μm can be easily achieved. The used magnetic scanning system allowed the beam to raster scan over custom square scanning areas over the horizontal (x) and vertical (y) directions with a step of ∽5 μm, and to know, for each recorded event, the beam position inside the scanning area. During the experiment, the scanning areas were centered on the different inter-strip regions to be studied. The size of the scanning area was typically 450 × 450 μm^2. The beam scanning and the detector positioning were controlled by means of the SPECTOR software [19].

2.2. DSSSDs and signal processing

The DSSSDs examined in the present study are model W1, manufactured by Micron Semiconductor Ltd, with declared thickness of 75 and 998 μm. Their area is 50×50 mm^2 and each side is divided into 16 parallel strips 3 mm wide. The junction (front) side is p-type and the ohmic (back) side is n-type. The strips on the front side are perpendicular to the ones on the back side, giving a granularity of 16×16=256 square shaped pixels with an area of 3×3 mm^2.

They are built using a standard combination of implantation and photolithography techniques. The front and back side surfaces of a high-purity silicon wafer (n-type) are oxidised to create oxide layers (SiO_2). That are selectively removed by photolithography from the areas where active windows (strips) or p-stop layers will be located. The residual SiO_2 spacing between adjacent strips (i.e. the inter-strip gap width) is on the front side 100 μm wide and 0.9 μm thick (see figure 1a). The junction is formed by implantation of acceptor ions (p-type), using an accelerator. The back surface of the wafer is implanted with donor ions resulting in strips of n^+ material. To avoid a conducting path between n^+-n-n^+ structure, backside strips are isolated by a p-stop implantation 40 μm wide. Hence, the strip separation on the back side is 30 μm SiO_2, 40 μm p-stop and 30 μm SiO_2, resulting in the total value of 100 μm(see figure 1b). Finally a 0.3 μm thick Aluminum metalization layer, not overlapping with the SiO_2 regions, provides thin ohmic electrical contacts of the strips at both sides. The silicon dead layer, due to the implantation process, has a nominal thickness of 0.5 μm (see figures 1 a and b). The full-depletion voltages declared by the manufacturer for the thick and thin detectors are 180 V and 3 V, respectively.

In the experiment presented in this paper, the DSSSDs were mounted under vacuum ($\approx 10^{-6}$ mbar) in the nuclear microprobe station in a such way that protons enter the detectors always from the front side. Furthermore, detectors were mounted with the front strips parallel to the vertical direction and the back strips parallel to the horizontal direction. In the following, we will use the names F0 to F15 to indicate the 16 front strips and B0 to B15 to indicate the 16 back strips.

The electronics was assembled in such a way to allow for the simultaneous recording of signals of both polarities from all strips. The signals from the strips were processed by MESYTEC MPR 16 pre-amplifiers, SILENA 716 programmable amplifiers and SILENA 9418 ADCs. The shaping time of the amplifiers was set to 0.5 μs. The acquisition system was triggered by a total OR of the logic signals related to all the 32 strips. Each recorded event consisted of the coordinates (x, y) corresponding to the horizontal and vertical beam

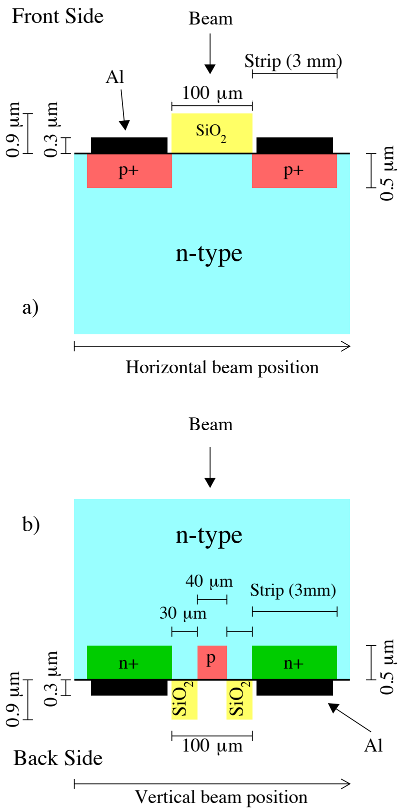

Figure 1: (Colour online) Schematic layout of the inter-strip region of the DSSSD. a) Cross-section of the electrode structure of the front side; b) The same for the back side. The drawing is schematic and not to scale.

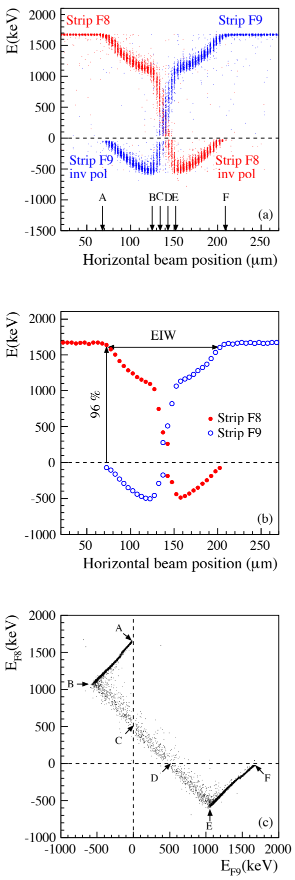

Figure 2: (Colour online) a) Energy signal amplitude profiles for the front strips F8 (red points) and F9 (blue points) of the 998 μm thick DSSSD, over-depleted at 270 V, with the beam scanning area centered on the front inter-strip F8-F9 and for a proton energy of 1700 keV. b) Same as figure 2a but averaged data. The definition of the effective inter-strip width (EIW, see text) is also sketched in the figure. c) Energy correlation F8-F9 for the events of figure 2a. Letters indicating different points in the F8-F9 correlation plot correspond to the ion impact position indicated in figure 2a. See text for further details.

position inside the scanning area and 64 energy signals (normal and inverted polarity for each strip) from all the front and back strips.

In the experiment, the inter-strip effects were investigated by raster scanning over different inter-strip regions of the front and back side, in order to study the correlation between the energy measured from two adjacent strips and the impact position of the incoming particles. An example of such correlation is shown in figure 2. Here one can see the energy signal amplitudes as a function of the horizontal position (energy signal amplitude profiles in the following) from the front strips F8 and F9 when a proton beam of energy 1700 keV irradiates the 998 μm thick detector operating in over-depletion at 270 V. When the beam hits only strip F8 (i.e. far from the inter-strip region, impact position on the left of point A), complete charge collection and thus full energy detection is achieved. When the beam approaches the left side of the inter-strip gap, the normal polarity F8 signal decreases and, at the same time, inverted polarity signals appear in F9 (region between points A and B) reaching a maximum value at position B. Moving toward the center of the inter-strip, the F9 inverted polarity signals decrease (region between point B and C) and reverts to zero at position C. In the center of the inter-strip gap both strips produce normal polarity pulses (region between points C and D) but with reduced amplitude. In the right half-side of the inter-strip region, the behaviour is symmetrical. The F8 signal reaches zero at point D and inverted polarity signals occur in the region between points D and E, reaching their maximum at point E. Finally, in the region between points E and F the F8 inverted polarity signal amplitude decreases to zero while the normal polarity signal of strip F9 monotonically increases up to the full energy measured, which is reached at point F.

Since the effective width of the inter-strip gap is different from the geometrical one declared by the manufacturer, our aim was to study how such region, which in turn is related to the DSSSD efficiency for full deposited energy detection, depends on the operating conditions, such as detector bias and proton energy. With the aim to compare the results of the various measurements, we transformed the raw data, as the ones in figure 2a into averaged values of position and energy, as the ones in figure 2b. Data are sorted in steps of 5 μm with an estimated position uncertainty of ±2.5 μm. For each position, the mean value of the measured energy and its error were calculated from the recorded data. In this paper we define the effective inter-strip width (EIW) as the difference between the two beam positions where the energy signals from the two adjacent strips drop below 96% of their full amplitude (see figure 2b). The threshold of 96% was arbitrarily chosen to enable comparison of all the different shapes of the averaged plots, including those obtained with the thin detector.

We recall that, in previous papers, such inter-strip effects for charged particle detection have been studied by observing energy correlations between adjacent strips e.g. [11, 14, 15]. Such a correlation plot for the data of figure 2a is shown in figure 2c, which is similar to the ones observed in e.g. [11, 14, 15]. As shown in figure 2c, the spatially resolved IBIC measurements of charge pulses allowed, for the first time, to clearly associate different points of the F8-F9 correlation plot with the entrance coordinates of the incoming ion.

3. Experimental results

The response of the two DSSSDs was studied at different bias voltages: under-depleted, fully-depleted and over-depleted. Because of the different behaviour of the two detectors, the results will be presented separately in the following two sub-sections.

3.1. Results for the 998 μm thick DSSSD

In these measurements proton micro-beams of incident energies 1700 and 6000 keV hit the surface of the detector around a front or a back inter-strip region. Results presented in figure 3 concern the measurements with a proton beam of energy 1700 keV and a scanning area centered on the front inter-strip F8-F9 and on the center of strip B7. Bias voltages equal to 0.5, 1.0 and 1.5 times the full-depletion one were used. Increasing the bias, the detector response improves both for the front and back side strips, leading to a decrease of both

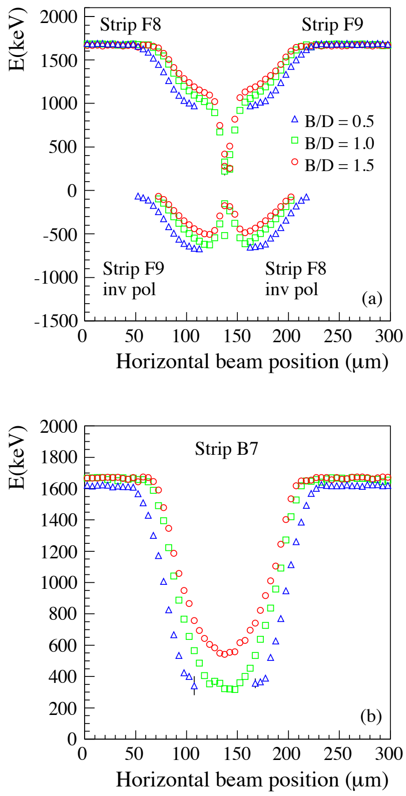

Figure 3: (Colour online) Energy signal amplitude profiles for the 998 μm thick DSSSD with a proton beam energy of 1700 keV and a scanning area centered on the front inter-strip F8-F9 and on strip B7. B/D indicates the ratio between the applied bias and the full depletion voltage. a) Inter-strip behaviour for strips F8 and F9. b) Strip B7 response versus the horizontal beam position.

the inverted polarity pulse amplitudes and the EIW. Figure 3b clearly shows that, although the scanning area is centered on strip B7, when the incoming protons cross the front inter-strip region, one has a reduced signal on B7. In such conditions no signals are observed on back strips different than B7 for all the tested B/D values. It is worth noting that, according to the charge conservation principle, the measured back strip signal amplitude equals the sum of the pulses from the two front strips (taking into account their polarities), thus confirming the reliability of the energy calibration [20, 21].

Figure 4 presents results of the measurements with a proton beam energy of 1700 keV and a scanning area centered on the back inter-strip B6-B7 and on front strip F9. Contrary to the front inter-strip case, inverted polarity pulses were not observed in all performed measurements as function of detector bias and beam energy. For an over-depleted and fully-depleted detector the EIW is about twice the declared geometrical width of the inter-strip gap, and in under-depleted conditions (blue empty triangles in figure 4a), this area considerably increases. Our results confirm the observation [11] that the sum of the two signals from adjacent back strips provides the correct full energy information for back inter-strip events, if the incoming particle is not crossing the front inter-strip. In all of these measurements the front strip generates the expected full energy signal as it is shown in figure 4b.

Figure 5 summarizes the dependence of the measured front and back EIWs, on the bias voltage for different beam energies. The overall behaviour is that both the front and back EIWs decrease by increasing the bias voltage. Black full circles and blue full triangles correspond to proton energies of 1700 keV and 6000 keV, respectively, for the same front inter-strip and show that the front EIW for protons at 6000 keV is significantly smaller than the one for protons at 1700 keV. The red empty circles correspond to the results obtained for the back inter-strip at a proton energy of 1700 keV. As one can see on the right Y scale of figure 5, the EIW can be significantly different than the geometrical inter-strip width. At a beam energy of 6000 keV the protons stop inside the detector at depth of 295 μm, quite far from the detector surface, resulting in

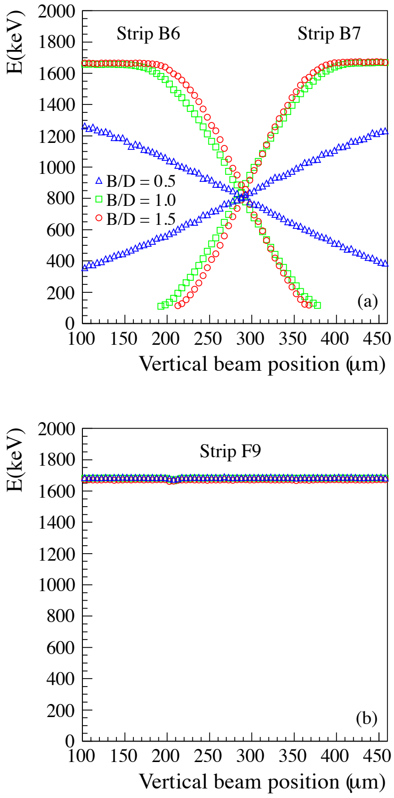

Figure 4: (Colour online) Energy signal amplitude profiles measured with a proton microbeam of 1700 keV and a scanning area centered on the back inter-strip B6-B7 and on the center of strip F9. B/D is the ratio between the bias and the full depletion voltage. a) Energy response of the back strips versus the vertical beam position. b) F9 strip response versus the vertical beam position.

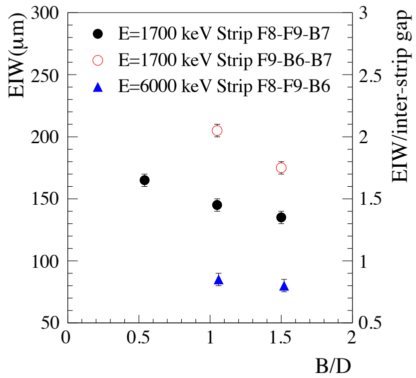

Figure 5: (Colour online) EIW dependence on the ratio between bias voltage and full depletion voltage (B/D). The axis on the right side shows the ratio between the EIW and the declared geometrical width of the inter-strip gap. F8-F9-B7: beam on inter-strip F8-F9 and center of strip B7. F9-B6-B7: beam on inter-strip B6-B7 and center of strip F9. F8-F9-B6: beam on inter-strip F8-F9 and center of strip B6.

a reduced effective front inter-strip width. On the contrary, 1700 keV protons stop at a depth of only 35 μm, close to the junction side, and an enhanced EIW is observed.

In figure 3b it is shown that for ions passing through the front inter-strip region, even when a trajectory is passing through the center of a back strip, one observes a reduced back signal. With the aim to quantify this phenomenon, we consider the ratio between the minimum energy response (E_{min}) of the back strip and the full energy response (E_{full}) of the back strip observed when the beam hits the detector far from the inter-strip gap. The E_{min} value was obtained as the vertex of the parabola fitting the averaged data, and the corresponding error was calculated from the parameters obtained from the fit. This procedure allowed to extract the E_{min} value also for B/D=0.5 were, as shown in figure 3b, a few experimental points in the inter-stip center are missing. Figure 6 shows the dependence of $E_{min}/E_{full}(\%)$ on the ratio between bias voltage and depletion voltage. The plot shows that for low energy protons, stopped close to

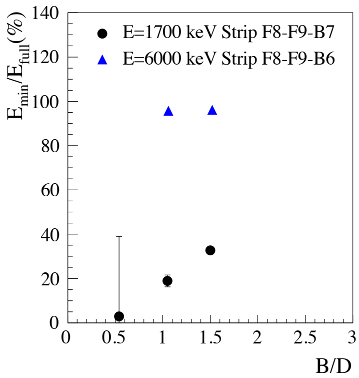

Figure 6: (Colour online) Plot of the ratio $E_{min}/E_{full}(\%)$ versus the ratio between bias voltage and full depletion voltage (B/D) for the thick DSSSD. F8-F9-B7: beam on inter-strip F8-F9 and center of strip B7. F8-F9-B6: beam on inter-strip F8-F9 and center of strip B6. See text for details.

the detector surface, a small ratio $E_{min}/E_{full}(\%)$ is observed.

Another measurement was also performed aiming to investigate the detector response to 1700 keV protons hitting the guard-ring in full depletion working conditions. Figure 7 shows the energy response of strip F8 (red points) when the scanning micro-beam moves along the vertical direction towards the guard-ring (decreasing vertical values). This plot shows that the signal amplitude in strip 8 gradually decreases when approaching the region between F8 and the guard-ring. At the same time, when the ions hit the detector volume at the guard-ring position, an induced signal appears on strips F0 and F15. These are the two outermost front strips and they are surrounded by the guard-ring. No induced signals are observed on the other front strips. We interpret this latter observation as due to the strong capacitive coupling between the outermost strips and the guard-ring. A similar behaviour is found also for the thin detector. The guard-rings of both used detectors were floating with no connection to the detector multipin connector.

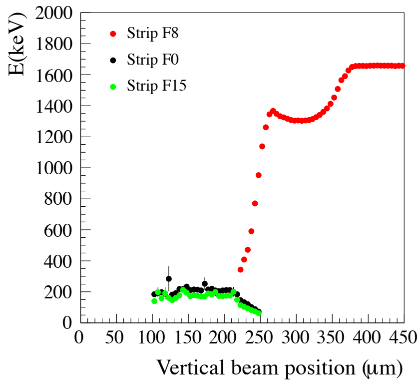

Figure 7: (Colour online) Detector response observed with a proton micro-beam of 1600 keV moving in the vertical direction along strip F8. When ions approach the region between F8 and the guard-ring, the F8 signal decreases and induced signals appear in F0 and F15 (see text for details).

3.2. Results for the 75 μm thick DSSSD

In these measurements proton micro-beams of incident energies 800, 1700 and 3000 keV hit the front surface of the detector around the front or back inter-strip regions. In figure 8 are presented results for the DSSSD irradiated by protons of 1700 keV for three different bias conditions. The scanning area was centered on the front inter-strip F6-F7 and on the center of back strip B8. Surprisingly, in this case inverted polarity pulses are recorded only in over-depleted working conditions (see red empty circles in figure 8).

By using the method described in section 2.2, the EIW has been extracted for different working conditions. Figure 9a shows the front EIW as a function of B/D up to a B/D value of 2.9 which we do not have for the thick detector case. As one can see, the front EIW shows a non-monotone trend as function of the polarization voltage and a region, close to the nominal full-depletion voltage value, where the EIW value is minimum.

Figure 9b presents the results for the back EIW. The trend is similar to the

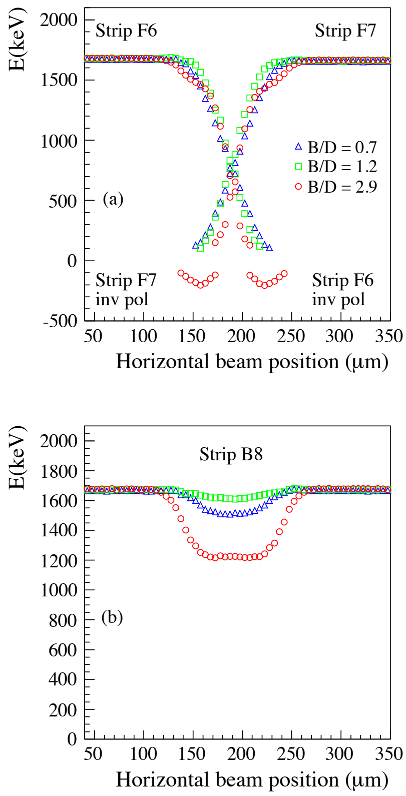

Figure 8: (Colour online) Energy signal amplitude profiles of the 75 μm thick DSSSD for protons of 1700 keV and a scanning area centered on the F6-F7 inter-strip and back strip B8. a) Response of F6 and F7 versus the horizontal beam position for three different bias voltages. b) B8 strip response versus the horizontal beam position. For comparison see figure 3, showing the results of identical measurements for the thick detector.

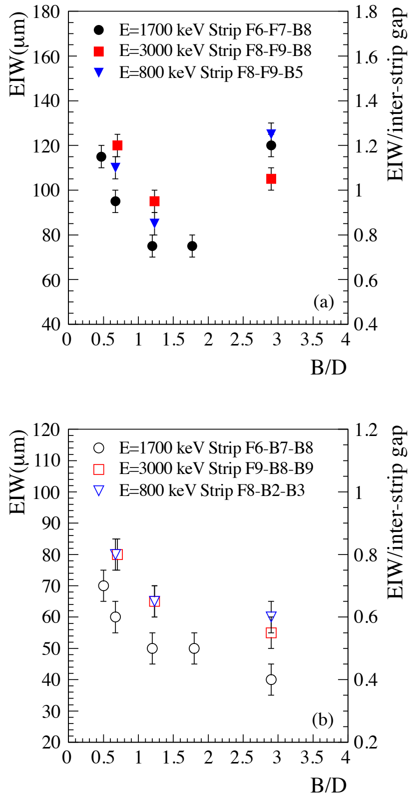

Figure 9: (Colour online) Dependence of the effective inter-strip width on the ratio bias voltage/depletion voltage for the 75 μm thick DSSSD. a) Front inter-strip behaviour. F6-F7-B8: beam on inter-strip F6-F7 and center of strip B8. F8-F9-B8: beam on inter-strip F8-F9 and center of strip B8. F8-F9-B5: beam on inter-strip F8-F9 and center of strip B5. b) Back inter-strip behaviour. F6-B7-B8: beam on inter-strip B7-B8 and center of strip F6. F9-B8-B9: beam on inter-strip B8-B9 and center of strip F9. F8-B2-B3: beam on inter-strip B2-B3 and center of strip F8.

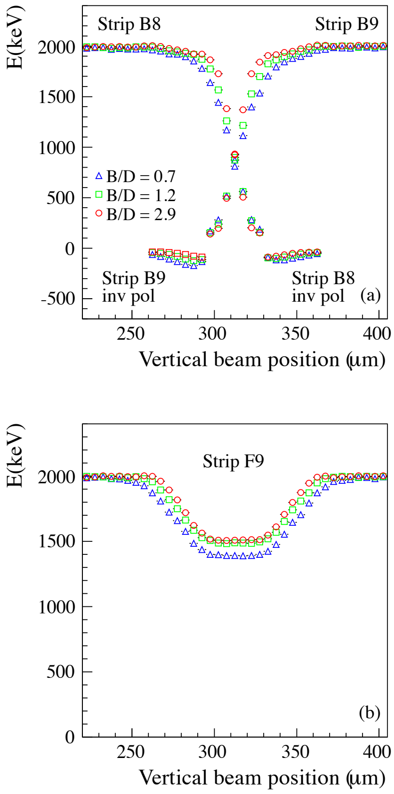

Figure 10: (Colour online) Energy signal amplitude profiles for the 75 μm thick DSSSD with 3000 keV protons, punching through the detector, and a micro-beam scanning area centered on the back inter-strip B8-B9 and on strip F9. a) Behaviour of the B8-B9 back inter-strip. b) strip F9 response as a function of the vertical beam position.

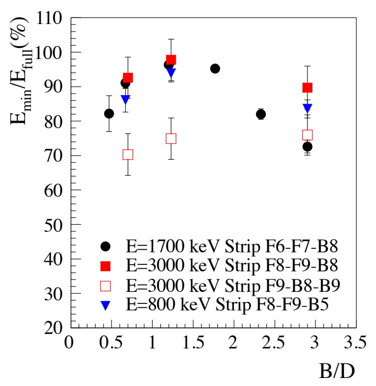

Figure 11: (Colour online) Plot of the ratio $E_{min}/E_{full}(\%)$ versus the ratio bias voltage/depletion voltage for the thin DSSSD. F6-F7-B8: beam on inter-strip F6-F7 and center of strip B8. F8-F9-B8: beam on inter-strip F8-F9 and center of strip B8. F9-B8-B9: beam on inter-strip B8-B9 and center of strip F9. F8-F9-B5: beam on inter-strip F8-F9 and center of strip B5. See text for details.

thick detector (red empty circles in figure 5). The back EIW decreases with increasing bias voltages, but the overall values are smaller than those measured for the thick detector.

The thin detector enables measurements of the detector response for incident protons punching through the DSSSD, new mode inaccessible in the measurements with the 998 μm thick detector for which protons are stopped in the DSSSD for all the available beam energies. The observed front inter-strip response in the punch-through condition, with protons of 3000 keV, is similar to that presented in figure 8 for lower beam energies when protons are stopped inside the DSSSD. On the contrary, the back inter-strip behaviour, shown in figure 10, is quite different. In fact, inverted polarity signals are observed in the back strips for all bias conditions, with increasing amplitude for decreasing bias. Figure 10b clearly shows that even if the micro-beam scanning area covers the center of strip F9, if the incoming protons are crossing the back inter-strip region, the considered front strip has a reduced amplitude signal.

We report in figure 11 (the analogous of figure 6 for the 998 μm thick detector), the ratio between the minimum energy response (E_{min}) of the back (front) strip and the full energy response (E_{full}) of the back (front) strip. Since the trend of the signal amplitude as function of the position is not parabolic as for the thick detector, (E_{min}) corresponds to the mean value of the energy projection relative to the 'flat' region (see e.g. figure 10b). In this case, E_{min}/E_{full} shows a maximum around the full-depletion voltage value.

4. Model calculations and interpretation

Despite a full numerical modeling of the devices under investigation is beyond the scope of the present work, a simplified simulation based on the Shockley-Ramo-Gunn framework is presented in the following subsections in order to provide a qualitative interpretation of the experimental findings. Since the whole simulation and interpretation depends on the electrostatic configuration of the device and on the interpretation of the induced charge pulse signals, such topics will be discussed first in the general case in subsections 4.1 and 4.2. The formation of inverted polarity signals will then be discussed in subsection 4.3. Finally, in the remaining subsections, the previously presented experimental results will be compared with the results of the simulations.

4.1. Interpretation framework

In a system at the electrostatic equilibrium with an arbitrary arrangement of N electrodes, the instantaneous current i_i induced at the i-th electrode by the motion of a point charge q in the detector volume, can be expressed as [22]:

$$i = -q\overrightarrow{v} \cdot \overrightarrow{E}_{w,i} \tag{1}$$

where $\overrightarrow{v}$ is the velocity of the charge carrier and $\overrightarrow{E}_{w,i}$ is the weighting field associated with the i-th read-out electrode considered. The electric field determines the charge trajectory and velocity. The weighting field, relates the motion of the charge carriers to the current induced at the read-out electrodes. The weighting field can be expressed in terms of the weighting potential ψ_w:

$$\overrightarrow{E}_{w,i} = -\overrightarrow{\nabla}(\psi_{w,i}) \tag{2}$$

where the weighting potential can be written as the derivative of the electric potential ψ with respect to the voltage applied at the read-out electrode [23, 24]:

$$\psi_{w,i}(\overrightarrow{x}) = \frac{\partial \psi(\overrightarrow{x})}{\partial V_i} \tag{3}$$

The time integration of eq. 1 shows that the total charge induced by q at the i-th read-out electrode is proportional to the difference in weighting potential between its value at the initial position $\overrightarrow{x_a}$, where charge carriers are generated, and at its final position $\overrightarrow{x_b}$ [25]:

$$Q_i = q \cdot (\psi_{w,i}(\overrightarrow{x_b}) - \psi_{w,i}(\overrightarrow{x_a})) \tag{4}$$

It is worth noting that, the position $\overrightarrow{x_b}$ can be either the collecting electrode or another position within the detector volume, where trapping or recombination occurred. The signal amplitudes, measured in the present experiment, are proportional to the total induced charge Q in the considered read-out electrode which is obtained by the time integration of the induced current pulse. Therefore, the combination of the charge transport properties of the detector material, the geometry and topology of the electric field and of the weighting potential, define the response of the DSSSDs under investigation for a given incident ion and energy.

4.2. Calculation of induced charges

A qualitative numerical analysis for the DSSSDs configurations under investigation was implemented performing simplified calculations of the electric field and the weighting field. A 200 µm wide cross section of the devices was simulated both for the front and back inter-strips of the 75 µm and the 998 µm thick detectors. For simplicity, simulations were performed assuming an isolated system of three electrodes and neglecting any coupling with the remaining strips.

Simulations were performed by means of the commercial finite element method (FEM) solver Comsol Multiphysics 4.3 [26]; using the device specifications given by the manufacturer, maps of the electric potential, weighting potential and electric field stream lines for different values of applied voltage were obtained. Numerical simulations were performed as follows. The electric potential ψ calculation was defined by the FEM solution of the Poisson's equation coupled with the carriers stationary drift-diffusion equation:

$$\left.\begin{array}{l} -\epsilon\,\nabla^2\psi(\overrightarrow{x}) = q\left[N_D(\overrightarrow{x}) - N_A(\overrightarrow{x}) - n(\overrightarrow{x}) + p(\overrightarrow{x})\right] \\ \nabla\cdot\left[D_n\nabla n(\overrightarrow{x}) + \mu_n\nabla\psi(\overrightarrow{x})n(\overrightarrow{x})\right] = 0 \\ \nabla\cdot\left[D_p\nabla p(\overrightarrow{x}) - \mu_p\nabla\psi(\overrightarrow{x})p(\overrightarrow{x})\right] = 0 \end{array}\right\} \quad (5)$$

where p and n are the hole and electron concentrations, N_D and N_A represent the donor and acceptor concentrations, $D_{n,p}$ and $\mu_{n,p}$ indicate the carriers diffusivity and mobility, respectively.

In order to describe the static equilibrium, the steady state was considered in the continuity equations by neglecting any transient effect $\partial n/\partial t = \partial p/\partial t = 0$ and by setting an infinite recombination time for both charge carriers. Considering Poisson's equation, Dirichlet boundary conditions $\psi(\overrightarrow{x}_j) = V_j$ were set at the electrodes, and Neumann conditions were assumed elsewhere. A surface charge density σ was also defined at the oxide interfaces. Considering electron and hole concentrations, Dirichlet boundaries $p(\overrightarrow{x}_j) = 0$ and $n(\overrightarrow{x}_j) = 0$ were assumed at the front electrodes, and $p = N_A$, $n = N_D$ at the back electrodes. The $p^+ - n$ junction formed by the p-stop at the center of the back inter strip was simulated imposing a Dirichlet boundary condition $n(\overrightarrow{x}) = 0$ on the electron continuity equation. Neumann boundary conditions were assumed elsewhere.

After the electric field calculation, the weighting potential $\psi_{w,j}$ was then evaluated according to the prescriptions in eq. 4 and in [23, 24]. Defining, for ease of writing,

$$\frac{\partial\psi}{\partial V_j} = \psi_{w,j} \quad \frac{\partial n}{\partial V_j} = \nu_j \quad \frac{\partial p}{\partial V_j} = \pi_j \quad (6)$$

where j=1,2,3 is the electrode index, and assuming any other parameter in eq. 5 (mobility, diffusivity and dopants concentration) as independent on the applied bias, then the voltage differentiation of eq. 5 provides a new set of differential equations, written in terms of the weighting field of the read-out electrode:

$$\left.\begin{array}{l} -\epsilon\nabla^2\psi_{w,j}(\overrightarrow{x}) = q\cdot[\pi_j(\overrightarrow{x}) - \nu_j(\overrightarrow{x})] \\ \nabla\cdot[D_n\nabla\nu_j(\overrightarrow{x}) - \mu_n\nabla\psi(\overrightarrow{x})\nu_j(\overrightarrow{x}) - \mu_n\nabla\psi_{w,j}(\overrightarrow{x})n(\overrightarrow{x})] = 0 \\ \nabla\cdot[D_p\nabla\pi_j(\overrightarrow{x}) + \mu_p\nabla\psi(\overrightarrow{x})\pi_j(\overrightarrow{x}) + \mu_p\nabla\psi_{w,j}(\overrightarrow{x})p(\overrightarrow{x})] = 0 \end{array}\right\} \quad (7)$$

where $i \neq j$ and ψ is the solution of eq. 5. Dirichlet boundary conditions associated with eq. 7 were defined as

$$\psi_{w,j}(\overrightarrow{x}_k) = \delta_{j,k} \quad \nu_j(\overrightarrow{x}_k) = 0 \quad \nu_j(\overrightarrow{x}_k) = 0 \quad (8)$$

where j is the index of the read-out electrode and k is a generic electrode index. Neumann boundary conditions were assumed elsewhere.

In figure 12, the weighting potential maps associated with the read-out electrode ($\mathrm{F_i}$ for the front and $\mathrm{B_i}$ for the back) are presented for the two DSSSDs at the nominal full depletion configuration (B/D=1), in absence of any surface charge densities at the oxide interface. The internal electrostatic properties of the DSSSDs under investigation are similar, from a topological point of view, to those of other devices or analogous multi-electrode structures previously studied in references [8–10, 15, 27].

To summarize, we consider a sub-system of the DSSSD consisting of three electrodes for the front inter-strip (figure 12 a and c): two adjacent front strips biased at negative voltage ($\mathrm{F_i}$, $\mathrm{F_j}$, where $\mathrm{F_i}$ is the read-out electrode) and one grounded back strip $\mathrm{B_s}$. In such a sub-system the electric field stream lines originating from $\mathrm{B_s}$ diverge from the median inter-strip coordinate x_0, and they sink either at the left $\mathrm{F_i}$ or right $\mathrm{F_j}$ front strip. At the front side, the weighting potential decreases from $\mathrm{F_i}$ (where $\psi_{w,i} = 1$) to $\mathrm{F_j}$ (where $\psi_{w,i} = 0$), having a value lower than 0.5 at the median abscissa x_0. Similarly, the weighting potential decreases from 1 to 0 along the left edge of the cross section connecting $\mathrm{F_i}$ with the back strip $\mathrm{B_s}$.

A symmetric configuration of the weighting potential is assumed for the read-out electrode $\mathrm{F_j}$ with $\psi_{w,j} = 1$ at $\mathrm{F_j}$ and $\psi_{w,j} = 0$ at the $\mathrm{F_i}$ and $\mathrm{B_s}$ electrodes.

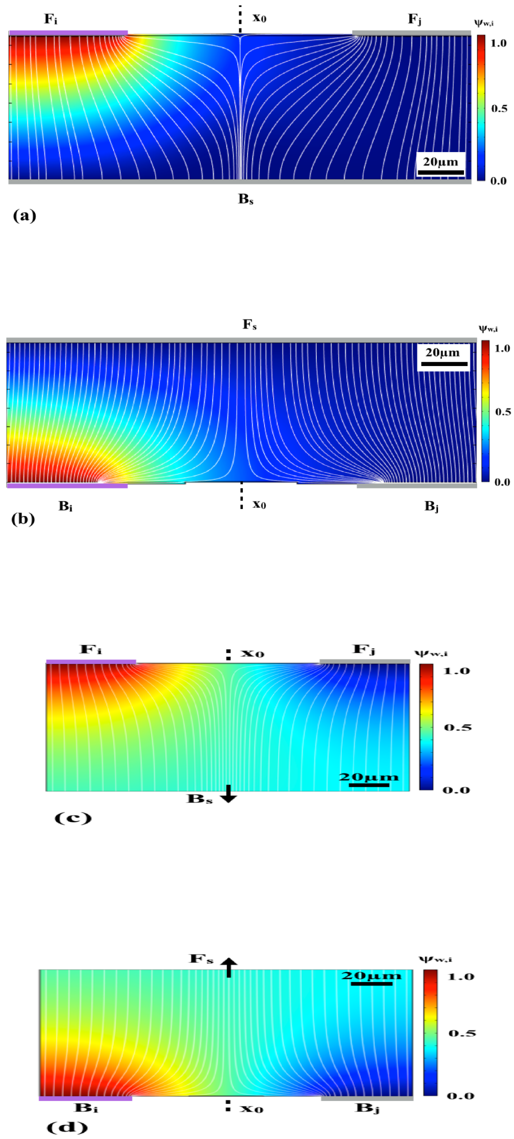

Figure 12: (Colour online). Simulated weighting potential maps (color scale on the right) and electric stream field lines (in white) at B/D=1 assuming zero surface charge at the Si-SiO_2 interface for: a) 75 μm detector, front inter-strip; b) 75 μm detector, back inter-strip; c) 998 μm detector, front inter-strip; d) 998 μm detector, back inter-strip. The read-out electrode, associated with the simulated weighting potential shown, is sketched in purple. The back electrode B_S in c) and the front electrode F_S in d) are out of the figure.

For completeness, we remind that the value of the weighting potential associated to the back strip B_s at a position $\vec{x}$ inside the detector volume $\psi_{w,s}(\vec{x})$ can be obtained by the charge conservation principle, for which at every position $\vec{x}$, the sum of the weighting potentials must be equal to one [21]. Therefore for our simplified system of three electrodes we have:

$$\psi_{w,s}(\vec{x}) = 1 - \psi_{w,i}(\vec{x}) - \psi_{w,j}(\vec{x}) \tag{9}$$

It is worth noting that in a non-isolated system the sum should extend to all the front and back electrodes of the detector. Similar considerations hold for the back inter-strip electrostatics (figure 12 b and d), provided that the electric field stream lines originate from the two back strips B_i, B_j and sink at the front strip F_s. The evaluated electric field stream lines and weighting potential distribution show qualitatively the same topological configuration for the 75 µm and 998 µm thick detectors.

4.3. Origin of inverted polarity pulses

An interpretation of the induced charge pulse formation is proposed, based on the results presented in figure 12. The charge induction mechanism is described according to eq. 4. Considering the creation of an electron-hole pair in the front inter-strip gap (e.g., figure 12a and c), the motion of both charge carriers will induce three concurrent signals on F_i, F_j and B_s. Assuming for simplicity that the charge carriers are created close to the front surface, the electron moves towards the back strip, where both j-th and i-th weighting potentials are zero, thus inducing a positive signal on F_i and F_j according to eq. 4; the absolute value of the signal induced on B_s will be given, according to eq. 9 and eq. 4, by the sum of the signals induced at the front electrodes. On the other hand, according to the electric field distribution, the hole drifts towards F_i or F_j depending on its generation position. As an example, an hole created in the right side of the inter-strip region will move towards strip F_j; considering the weighting potential distribution, the hole will therefore induce a normal (positive) polarity pulse on F_j and an inverted (negative) polarity pulse on F_i according to eq.4 [21]. Thus, if all holes are collected by F_i and all electrons are collected by the back strip B_s, both electron and hole induce positive polarity current signal on strip F_i and the sum of the two contributions will correspond to the full energy amplitude detected. On the other hand, as the signal induced on F_j by the hole collected at F_i has negative polarity, the result is a bipolar induced current at F_j. However, when all the produced charge carriers are collected by F_i and B_s, the time-integration of the induced current signal on F_j gives a total charge equal to zero and the inverted polarity hole signal on F_j cancels out with the electron contribution. However, a non-zero inverted-polarity charge can be induced on the strip F_j if electrons are trapped or recombine along their path, preventing the full collection at the back strip B_s [15, 21]. In the above discussion we understood that, the occurring of anomalous polarity pulses can be always regarded as a consequence of charge losses within the active volume of the device.

Particularly, in [8, 9] the occurring of inverted polarity pulses was investigated in detail in terms of the presence of a local potential maximum, as well as of radiation-induced damage at the Si-SiO_2 interface. In the model proposed in [21], inverted polarity pulses could occur if the time-integration of the bipolar induced current does not fall to zero, i.e. if the positive contribution due to one carrier species (electrons) is not sufficient to cancel out the inverted polarity current generated by the other one (holes). This is ascribed in the model to a negligible electron lifetime in the device under test in [21] with respect to that of holes.

In the present case the good energy resolution and low leakage currents, show that the radiation damage of the detectors if present is at a minor level, both at the oxide interface and in the silicon bulk. Moreover, a large difference in the carriers lifetime, as that proposed in [21], is not suitable to fit the typical charge transport properties of high-purity silicon devices and could be considered only in the case that the manufacturing process would significantly modify the inter-strip detector bulk structure and geometry. A reasonable interpretation of charge losses in the DSSSDs under test is that a significant bending of the electric field lines occurs at the front and back inter-strip silicon-oxide interface, due to the build-up of an effective surface charge density, as suggested in [15]. Such an interpretation will be at the basis of the numerical simulations discussed in the following, concerning the interaction of protons, injected from the junction side, on the detectors. Due to the different configuration of front and back inter-strip, the discussion is subdivided into two separate subsections.

4.4. Front inter-strip simulation

The simple model we implemented to investigate the effects of a charge build-up at the Si-SiO_2 interface of the front inter-strip, is based on considering an effective positive surface charge density σ over the whole SiO_2 layer. The surface charge density was assumed to be constant on the whole interface. The device modelling consisted of performing a parametric sweep over the charge density value up to $\sigma = e \times 10^{10} cm^{-2}$, where e is the elementary charge, in order to obtain a reasonable agreement with the experimental data. The amplitude of the signals at the different considered electrodes, proportional to the induced charge at the considered electrode, was obtained taking into account the ionization profiles of the incoming protons evaluated by means of the Monte Carlo code SRIM [28]. In the following, results are discussed separately for the two devices under test.

4.4.1. Results for the 998 μm detector

A qualitative agreement with the experimental data was obtained assuming a positive charge density at the front Si-SiO_2 interface of $\sigma = e \times 5 \times 10^{9} cm^{-2}$. The relevant weighting potential and electric field stream lines of the 998 μm detector at B/D=1.0 are shown in figure 13 a. Assuming this value for σ , the applied voltage is not sufficient to prevent a bending of the electric field lines. Thus, the positive surface charge appears as a sink for the electrons generated within the first 20 μm in depth. Despite the significant simplifications assumed in the model, the signal amplitude profiles shown in figure 13 b evidence a qualitatively good description of the experimental profiles in figure 3 a. Particularly, the maximum value of inverted polarity pulse decreases from B/D=0.5, where it reaches ≈30 % of the deposited energy, to ≈15 % at B/D=1.5, in agreement with the experimental findings. Such a behaviour could be explained considering that the increase in the electric field strength, associated with the increase of the applied voltage, contributes to weaken the field stream lines bending towards the Si-SiO_2 interface, thus promoting the electron collection at the back electrode.

The simulated signal amplitude profile at the back electrode, for protons hitting the front inter-strip and the centre of the considered back strip, is shown in figure 14. As one can see, simulation results in figure 14 qualitatively reproduces the trend of the experimental data shown in figure 3 b, supporting once more the interpretation proposed above.

4.4.2. Results for the 75 μm detector

Unlike the case of the 998 μm detector, inverted polarity pulses were clearly measured in the 75 μm detector only in the over-depletion configuration with B/D=2.9. The simulated signal amplitude profiles are shown in figure 15 a for B/D values of 0.7, 1.2, 2.9. Simulations were implemented performing a sweep over the σ parameter at the Si-SiO_2 interface. The σ value corresponding to each B/D was chosen in order to obtain the best reproduction of the measured EIWs shown in figure 9 a and the obtained σ values are reported as a function of B/D in figure 15 b. The corresponding simulated EIWs, to be compared with the experimental values of figure 9a, are shown in figure 16. As one can see, in order to reproduce the data at B/D=2.9 (a B/D value which we do not have for the thick detector) we had to assume a value of the charge density σ considerably larger than for the other B/D values were the σ value is almost constant.

The field distribution in the case of B/D=2.9, simulated at the corresponding charge density shown in figure 15 b, is reported in figure 17.

In summary, the presence of inverted polarity pulses appears to be connected with the increase of positive surface charge at the front Si-SiO_2 interface for increasing applied voltage, in agreement with the interpretation of [15].

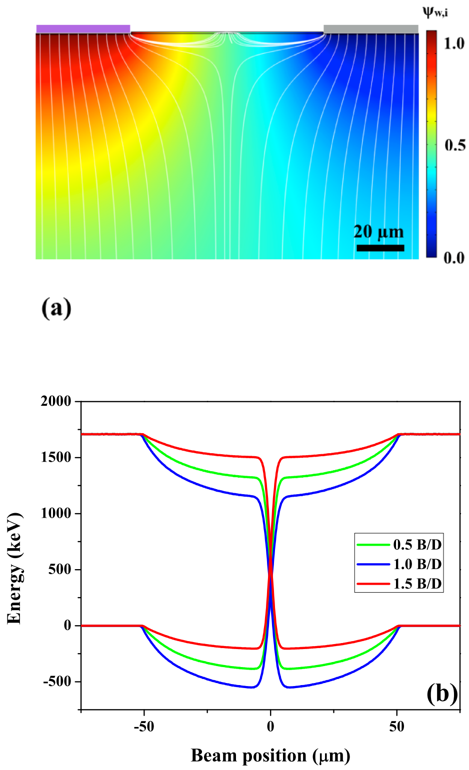

Figure 13: (Colour online) Simulated weighting potential map and electric field stream lines (in white) at B/D=1 for the front inter-strip of the 998 μm detector, where a uniform surface charge density $\sigma = e \times 5 \times 10^9 cm^{-2}$ was assumed. The read-out electrode, associated with the simulated weighting potential shown, is sketched in purple. b) Simulated energy signal amplitudes for 1700 keV protons as function of position along the front inter-strip assuming $\sigma = e \times 5 \times 10^9 cm^{-2}$. Beam position 0 corresponds to the center of the inter-strip.

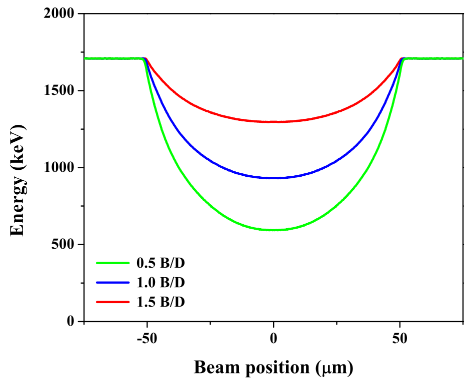

Figure 14: (Colour online) Signal amplitude profile of the back electrode of the 998 μm detector for front inter-strip events , simulated at different B/D assuming $\sigma = e \times 5 \times 10^9 cm^{-2}$ for 1700 keV protons. Beam position 0 corresponds to the center of the inter-strip.

4.5. Back inter-strip simulation

The same interpretation framework proposed for the front inter-strip, was assumed to hold for the qualitative analysis of the experimental results concerning the back inter-strip of the DSSSDs, provided that the role of holes and electrons is exchanged. For consistency with the interpretation of the front inter-strip results, we assume charge build-up in the two silicon-oxide interface layers in the back inter-strip, causing a local field reversal and acting as a sink for the electric field lines, thus preventing hole from collection at the front electrode. The simulations were performed implementing a parametric sweep of the σ values in the same range as that of the front inter-strip analysis. The p-stop at the center of the back inter strip, which is not connected to an external circuitry, was simulated by imposing a Dirichlet boundary condition on the electron continuity equation. Also in this case the analysis of the experimental data is subdivided into two separate subsections for the 998 μm and the 75 μm detectors.

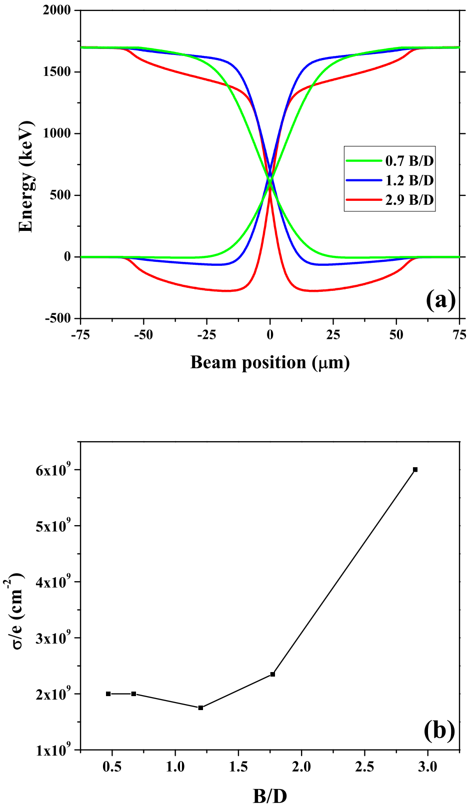

Figure 15: (Colour online) a) Simulated energy signal amplitudes for 1700 keV protons as function of position along the front inter-strip for the 75 μm detector at different B/D values. Beam position 0 corresponds to the center of the inter-strip. b) Best fitting values of σ/e as a function of B/D. See text for details.

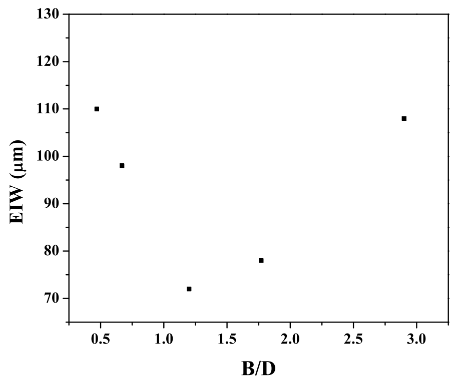

Figure 16: Simulated EIW values as function of B/D for the front inter-strip of the 75 µm detector.

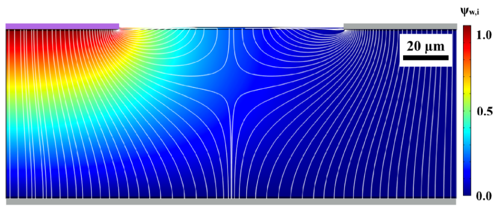

Figure 17: (Colour online) Simulated weighting potential maps (color scale on the right) and electric field stream lines (in white) for the 75 µm detector, considering B/D=2.9 and $\sigma = e \times 6 \times 10^9 cm^{-2}$.The read-out electrode, associated with the simulated weighting potential shown, is sketched in purple.

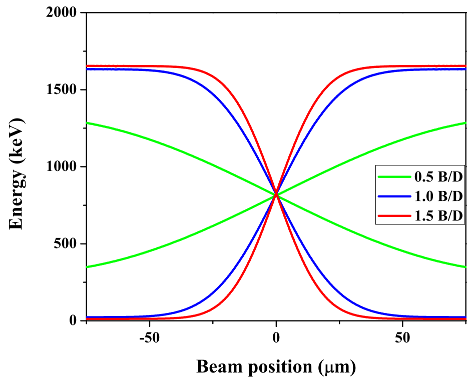

Figure 18: (Colour online) Simulated energy signal amplitudes for 1700 keV protons as function of position along the back inter-strip of the 998 μm detector for different B/D values assuming $\sigma = 0$. Beam position 0 corresponds to the center of the inter-strip.

4.5.1. Results for the 998 μm detector

The reference electrostatic configuration for the unperturbed device under test (i.e. σ=0) is depicted in figure 12 d. Recalling that the penetration depth of 1700 keV protons is about 35 μm, we can assume that the hole motion towards the front electrode is not affected by local modifications of the electric field lines at the back side. For this reason, the detection of charge losses and inverted polarity pulses is not expected in the present configuration. A parametric sweep over σ confirmed such an analysis, showing an insensitivity of the energy signal amplitude profiles in the $\sigma = \pm\ e \times 5 \times 10^9 cm^{-2}$ range. The simulated energy signal amplitude profiles, when the beam scans the back inter-strip region, are shown for different B/D in figure 18. In agreement with the lack of inverted polarity signals, the absence of charge losses is confirmed by the fact that summing the signals of two adjacent back strips one reproduces the amplitude of the full signal. The decrease of the EIW for increasing voltage is in qualitative agreement with the experimental findings shown in figure 4 a. When charge carrier generation occurs at several hundreds of micrometers above the back electrodes, the electron cloud size increases during the drift inside the detector bulk, contributing to the charge sharing between two adjacent back strips. Such an effect is more pronounced at low bias voltages, i.e. at 0.5 B/D. This phenomenon was shown in previous works on silicon and other detector materials (see e.g. [29, 30]). By increasing the bias voltage of the DSSSD, the strength of the electric field rises, leading to a reduction of the lateral diffusion of the charge carriers. The experimental decrease of the EIW for increasing voltage for the 998 μm detector, is in qualitative agreement with the present interpretation.

4.5.2. Results for the 75 μm detector

For protons of 1700 keV, the back inter-strip energy signal amplitude profiles are qualitatively the same as the ones of the 998 μm device, and are compatible with the previous discussion. In this case, the electron cloud travels on a shorter path than in the thicker detector; thus its lateral diffusion is less pronounced. Correspondingly, in agreement with the experimental findings, the simulated back EIW is smaller than the one of the 998 μm detector, as one can see comparing figures 18 and 19. Also in this case, a relative insensitivity to a surface charge density on the back side was observed, in the $\sigma = \pm\ e \times 5 \times 10^9 cm^{-2}$ range, for the energy signal amplitude profiles associated with 1700 keV protons, so that the unperturbed electric field distribution in figure 12 b is adequate to describe the present case. On the other hand, the inverted polarity pulses experimentally observed with a 3000 keV proton probe, having a penetration depth larger than the detector thickness, can be explained by assuming that a negative surface charge density is present at the back Si-SiO_2 interface. Simulated energy signal amplitude profiles at 3000 keV for different B/D values, shown in figure 20 a, were evaluated setting a constant negative surface charge density $\sigma = e \times 5 \times 10^9 cm^{-2}$ on the two back SiO_2 layers. The bending of the electric field stream lines associated with such a configuration, depicted in figure 20 b, is effective in causing the holes, generated within 20 μm above the back side, to drift towards the charged oxide interface.

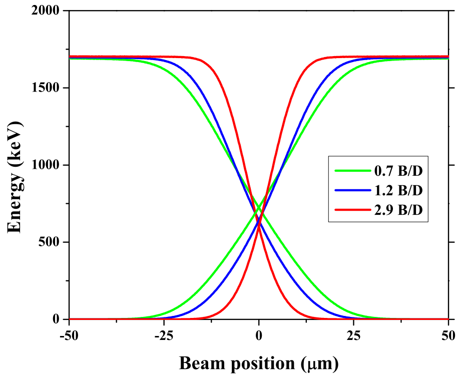

Figure 19: (Colour online) Energy signal amplitude profiles for the 75 µm detector back inter-strip, with 1700 keV protons and for different B/D values. Beam position 0 corresponds to the center of the inter-strip.

The qualitative agreement of the simulation predictions with the experimental data shown in figure 10 a, appears to support the present tentative interpretation for the charge signal formation mechanism in the back inter-strip. An interesting feature of both experimental findings and simulation results is that, differently from the results for the front inter-strip of the thin detector, the absolute value of the inverted-polarity signals decreases at increasing voltage. Such a behaviour is compatible with the assumption, which was implemented in the simulations, that the negative surface charge density is almost constant in the voltage range under investigation.

5. Summary and conclusion

A systematic study of the response of two DSSSDs of different thickness (75 and 998 µm) was performed by scanning the front and back inter-strip regions using proton micro-beams of different energies and for different detector bias voltages. Correlations between the position of the incoming ion and the signal

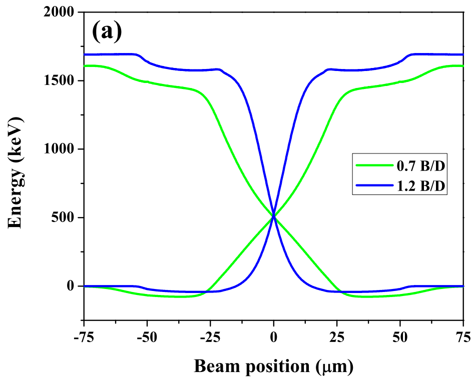

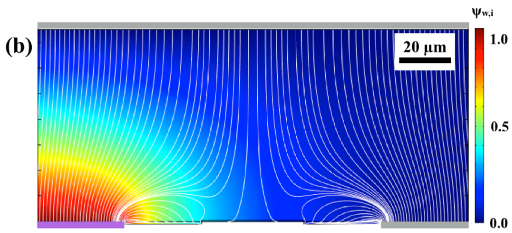

Figure 20: (Colour online) a) Energy signal amplitude profiles for the back inter-strip of the 75 μm detector with 3000 keV protons. Simulations were performed at different B/D assuming $\sigma = e \times 5 \times 10^{9} cm^{-2}$. Beam position 0 corresponds to the center of the inter-strip. b) Corresponding simulated weighting potential maps (color scale on the right) and electric field stream lines (in white).The read-out electrode, associated with the simulated weighting potential shown, is sketched in purple.

amplitude from the individual strips were studied using proton micro-beams of well defined size and trajectory. This allowed us to perform a systematic study of the behaviour of the effective inter-strip width, which is correlated to the DSSSD efficiency for full deposited energy detection, as a function of the operating conditions of each detector.

For the thick DSSSD the protons were always stopped inside the detector at all the available proton energies. In these conditions, signals of reduced amplitude are observed for the front inter-strip events, including inverted polarity ones. For back inter-strip events charge sharing between the two adjacent strips was observed, in absence of opposite polarity signals. The obtained results show that both front and back EIW can be much larger than the nominal width of the inter-strip gap and depend on the energy of the detected particles and on the polarization voltage.

The thin detector has been characterized both with protons stopping inside the DSSSD and in punch-through conditions. For protons punching through the detector, inverted polarity signals were clearly observed in the back inter-strip events for the first time.

The experimental observations were compared with the results of simplified simulations based on the Shockley-Ramo-Gunn framework. It was shown that assuming the build up of positive charge at the oxide interface in the front inter-strip and of negative charge at the oxide interface in the back inter-strip, one can obtain a satisfactory qualitative reproduction of all the observed inter-strip effects. A more complete analysis of the device, including additional details such as plasma effects, non uniformity of the surface charge density at the oxide interface or its dependence on the polarization voltage, might provide additional information but is beyond the scope of the present work.

In conclusion, the obtained results show that the front and back effective inter-strip widths, which are related to the DSSSD efficiency for full deposited energy detection, depend on the detector thickness and on the operating conditions. In addition, in [?] it has been shown that for detectors operated in atmosphere the inter-strip effects have a time dependence after biasing and, for detectors in dry atmosphere, steady state conditions can take days to be reached. Therefore, for detectors operating in high vacuum, as in the present case, a time dependence of the efficiency for full energy detection over the first days of measurement cannot be excluded. In summary, for those experiments aiming at accurately measuring quantities dependent on the efficiency for full energy detection, especially if two or more DSSSD are used in coincidence, a complete characterization of the used DSSSDs is required.

Acknowledgements

This work has been partly supported by the European Community as an Integrating Activity "Support of Public and Industrial Research Using Ion Beam Technology (SPIRIT)" under EC contract no. 227012.

Dr. Laura Grassi was employed through the European Community FP7 REGPOT project "Particle Detectors" (EC contract no. 256783).

The authors from Catania acknowledge the partial financial support of the Italian Ministry of Education and Research (PRIN 2010-2011, project 2010TP-SCSP)

The authors would like to thank the CHIMERA collaboration and INFN-LNS for providing equipments to perform the discussed measurements and Micron Semiconductor Ltd for providing information on the structure of the tested detectors.

References

[1] A. Di Pietro, et al., Physical Review C 85 (2012) 054607.

[2] M. Freer, et al., Journal of Physics G: Nuclear and Particle Physics 38 (2011) 115106.

[3] L. Acosta, et al., Physical Review C 84 (2011) 044604.

[4] A. Di Pietro, et al., Physical Review Letters 105 (2010) 022701.

[5] M. Freer, et al., Journal of Physics G: Nuclear and Particle Physics 37 (2010) 125102.

[6] D. Torresi, et al., International Journal of Modern Physics E 20 (04) (2011) 1026.

[7] M. Freer, et al., Physical Review C 84 (2011) 034317.

[8] T. Poehlsen, et al., Nuclear Instruments and Methods in Physics Research Section A 700 (2013) 22.

[9] T. Poehlsen, et al., Nuclear Instruments and Methods in Physics Research Section A 721 (2013) 26.

[10] T. Poehlsen, et al., Nuclear Instruments and Methods in Physics Research Section A 731 (2013) 172.

[11] D. Torresi, et al., Nuclear Instruments and Methods in Physics Research Section A 713 (2013) 11.

[12] S. Takeda, et al., Nuclear Instruments and Methods in Physics Research Section A 579 (2007) 859.

[13] V. Eremin, et al., Nuclear Instruments and Methods in Physics Research Section A 500 (2003) 121.

[14] Y. Blumenfeld, et al., Nuclear Instruments and Methods in Physics Research Section A 421 (1999) 471.

[15] J. Yorkston, et al., Nuclear Instruments and Methods in Physics Research Section A 262 (1987) 353.

[16] http://www.keithley.com.

[17] M. Jakšić, et al., Nuclear Instruments and Methods in Physics Research Section B 231 (2005) 502.

[18] M. Jakšić, et al., Nuclear Instruments and Methods in Physics Research Section B 260 (2007) 114.

[19] M. Bogovac et al., Nuclear Instruments and Methods in Physics Research Section B 267 (2009) 2073.

[20] Z. He, Nuclear Instruments and Methods in Physics Research A 463 (2001) 250.

[21] J. Forneris et al., EuroPhysics Letters 104 (2013) 28005.

[22] W. Shockley, Journal of Applied Physics 9 (1938) 635.

[23] E. Vittone, Nuclear Instruments and Methods in Physics Research B 219-220 (2004) 1043.

[24] L. A. Hamel, et al., Nuclear Instruments and Methods in Physics Research A 597 (2008) 207.

[25] V. Radeka, Annual Review of Nuclear and Particle Science 38 (1988) 217.

[26] COMSOL Multiphysics Available from: <http://www.comsol.com>

[27] J. Forneris et al., Nuclear Instruments and Methods in Physics Research B 306 (2013) 181.

[28] J.F. Ziegler et al., Nuclear Instruments and Methods in Physics Research B 268 (2010) 1818.

[29] V. Eremin et al., Journal of Instrumentation 7 (2012) C07002.

[30] J. C. Kim et al., Nuclear Instruments and Methods in Physics Research A 654 (2011) 233.